This is a preprint, the final version is subject to change, of the American Mineralogist (MSA)
Cite as Authors (Year) Title. American Mineralogist, in press.
(DOI will not work until issue is live.) DOI: http://dx.doi.org/10.2138/am-2015-5334

Revision 2

Hydrogrossular, $Ca_3Al_2(SiO_4)_{3-x}(H_4O_4)_x$: An Ab initio Investigation of its Structural and Energetic Properties.

Valentina Lacivita,[1,2,*] Agnes Mahmoud,[3] Alessandro Erba,[3] Philippe D'Arco,[2] and Sami Mustapha[4]

[1] *Institut du Calcul et de la Simulation, UPMC, Sorbonne Universités, F-75005 Paris (France)*

[2] *Institut des Sciences de la Terre Paris (UMR 7193 UPMC-CNRS), UPMC, Sorbonne Universités, F-75005 Paris (France)*

[3] *Dipartimento di Chimica and Centre of Excellence NIS (Nanostructured Interfaces and Surfaces), Università di Torino, via Giuria 5, IT-10125 Torino (Italy)*

[4] *Institut de Mathématiques de Jussieu (UMR 7586 UPMC-CNRS), UPMC, Sorbonne Universités, F-75005 Paris (France)*

[*] valentina.lacivita@upmc.fr

Abstract

Structural and energetic properties of the grossular-katoite solid solution are studied with a full *ab initio* quantum chemical approach. An all-electron basis set and the hybrid B3LYP functional are used. Calculations are performed within the primitive cell of cubic garnets. The hydrogarnet substitution, $SiO_4 \leftrightarrow H_4O_4$, yields 136 symmetry-independent configurations ranging from triclinic to cubic symmetry. All of them have been structurally optimized, the relaxed geometries being characterized by pseudo-cubic conventional cells. At the present level of approximation, the most stable configurations constitute by far the largest contributions to the system properties. Considering only the most stable configurations, average geometrical features of the actual solid solution are closely approximated. The excess volume displays a highly non-ideal behavior that is favorably compared with carefully analyzed and selected experimental data. The excess enthalpy deviates from the regular model; it draws an asymmetric function of composition with two minima that can be associated to structures or compositions observed in nature. Geometrical variations and distribution of the tetrahedra are analyzed. Calculations provide independent support to the use of a split-atom model for experimental refinements on these compounds. The asymmetry of the enthalpy of mixing can be associated with two distinct distribution patterns of the tetrahedra. Hydrogen interactions also contribute to the asymmetry of the excess enthalpy, as it turns out by comparison between compositions close to fully hydrated katoite and those close to grossular. Hydrogen interactions in Si-free katoite are found to be weak as suggested by dramatic changes in the H environment associated with the introduction of SiO_4 tetrahedra.

Keywords: hydrogarnet, hydrogrossular, grossular, hibschite, katoite, solid solution, *ab initio*, Crystal code

INTRODUCTION

Silicate garnets are nominally anhydrous minerals (NAMs) with stoichiometry $X_3Y_2(SiO_4)_3$, which, nonetheless, have been found to commonly contain hydrous components. Garnets characterized by a hydrous component fall under the general heading of hydrogarnets. They are crystalline solid solutions of general formula $X_3Y_2(SiO_4)_{3-x}(H_4O_4)_x$, whose composition varies through an isomorphous series from $x = 0$ to $x = 3$.

The main mechanism for hydrogen incorporation in silicate structures is through hydrogarnet substitution: $Si^{4+} \leftrightarrow 4H^+$. That is, protons are arranged in connection with four oxygen anions surrounding tetrahedral Si-free vacancies. The replacement of H for Si atoms was originally observed by Cohen-Addad et al. (1963) via nuclear magnetic resonance and neutron diffraction experiments on the fully hydrated synthetic sample $Ca_3Al_2(H_4O_4)_3$. Afterwards, numerous experimental studies on other hydrogarnets have confirmed this process (Aines and Rossman 1984, Cohen-Addad et al. 1967, Foreman Jr. 1968, Lager et al. 1989).

The incorporation of hydrous components into NAMs significantly affects their physical and chemical properties, thus modifying their technological applicability. Examples are the hydrolytic weakening of silicate materials for glass technologies (Griggs 1967), and the dielectric loss increase of ceramic substrates used as electronic packaging materials (Shannon et al. 1992). Changes in elasticity are also relevant to the properties of the Earth's mantle where they can hold relatively large amounts of "water" (Knittle et al. 1992, Mackwell et al. 1985, O'Neill et al. 1993).

Apparently, the hydration capability of garnets is directly related to the Ca content in the dodecahedral sites (X). Indeed, natural occurrences show ugrandites, $Ca_3(Al, Fe, Cr)_2(SiO_4)_3$, featuring "water" contents up to about 20 wt% (Passaglia and Rinaldi 1984), while pyralspites, $(Mg, Fe, Mn)_3Al_2(SiO_4)_3$, stand between 0.01 and 0.25 wt% (Aines and Rossman 1984). The analysis of synthetic samples confirms such differences (Ackermann et al. 1983, Cohen-Addad et al. 1963, Geiger et al. 1991). The key to interpretation was given by Sacerdoti and Passaglia (1985) while analyzing the structural response of grossular, $Ca_3Al_2(SiO_4)_3$, to hydrogarnet substitution: a progressive shortening of the octahedral-dodecahedral shared edge and a corresponding lengthening of the octahedral unshared edge was observed. This suggested a potential for substantial hydration only in those garnets whose anhydrous form displays a shared octahedral edge longer than the unshared one. By comparison between structures of various silicate garnet end-members previously

characterized (Novak and Gibbs 1971), they concluded that calcic garnets, i.e., garnets with ionic radius $r(\mathrm{X}) > 1$ Å, are the only ones that comply with such a requirement. Lager et al. (1989) later corroborated Sacerdoti and Passaglia's analysis with the results of distance-least-squares simulations on the effect of the hydrogarnet substitution on grossular, andradite and pyrope structures. They reasoned on a presumable effect of repulsion below some lower limit distance between the oxygen atoms involved in the shared edge: the minimum $\mathrm{O}-\mathrm{O}$ distance would be approached further along the shared edge of the anhydrous structure, and this may explain the high-water content of Ca-bearing garnets relative to other garnets. In addition, a remark is made to the fact that the eight-coordinated site widens as a consequence of the hydrogarnet substitution. According to Zabinski (1966), this effect should be energetically promoted by an X cation as large as Ca^{2+}, but rather hindered by smaller X cations, e.g., Mg^{2+} in pyrope.

A calcic hydrogarnet that occurs frequently in the literature is hydrogrossular, $\mathrm{Ca_3Al_2(SiO_4)_{3-x}(H_4O_4)_x}$, whose first reports date back to the early 1900s. In 1906, Cornu introduced the name hibschite for a new silicate mineral found at Marienberg, Bohemia, which, more than 30 years later, turned out to be hydrogrossular of ideal composition $\mathrm{Ca_3Al_2(SiO_4)_2H_4O_4}$ (Belyankin and Petrov 1941). The same conclusion was drawn by Pabst (1937) with regard to plazolite, a mineral named by Foshag (1920) in the aftermath of its first occurrence at Crestmore, California. In fact, hibschite and plazolite coincide, as was demonstrated by Pabst himself shortly after (1942). Today, the name plazolite has been abandoned; the official nomenclature adopts the name hibschite for identifying terms of the hydrogrossular series with $0 < x \leq 1.5$. Hydrogrossular with $1.5 < x \leq 3$ is called katoite, by the name assigned to the first natural sample of water-rich member of the series, $\mathrm{Ca_3Al_2(SiO_4)(H_4O_4)_2}$, found in Pietramassa, Italy (Passaglia and Rinaldi 1984). Figure 1 reports a graphical representation of the structure of hydrogrossular as a function of the substitutional fraction x of H for Si atoms.

Crystal chemistry and physical properties of hydrogrossular have been widely investigated due to important scientific and technological implications. As a typical product of cement hydration, katoite is of special concern to cement and concrete research for materials engineering. Fully-hydrated katoite, $\mathrm{Ca_3Al_2(H_4O_4)_3}$, is a recognized constituent of set Portland cement, and its composition often includes Si in mature cement pastes (Taylor and Newbury 1984). It is known that silica from various sources in cement can react with calcium and alumina ionic species to precipitate calcium aluminosilicate hydrates (Jappy and Glasser

1991). These are thermodynamically stable phases (Ackermann et al. 1983, Atkins et al. 1992, Bennett et al. 1992, Dilnesa et al. 2014) affecting rheology, solubility and global endurance of the material. For example, Flint and Wells (1941) found that siliceous katoite displays far greater resistance to the attack by sulfate solutions than the Si-free isomorphous form. This is relevant not only for civil construction purposes, but also in view of the employment of cement-based materials for the immobilization and containment of toxic wastes, such as radioactive waste repositories (Atkins and Glasser 1992). Hydrogrossular is a potential host phase for various toxic metals and metalloids, like Cr(VI). Evidence for chromate substitution in katoite, i.e., substitution of hydroxyl $[H_4O_4]^{4-}$ tetrahedra by chromate $[CrO_4]^{2-}$tetrahedra, has been provided (Hillier et al. 2007).

In Earth science, hydrogrossular is regarded as a likely "water" carrier in eclogite regions of the upper mantle. Spectroscopic studies performed on hibschite, up to 25 GPa pressure, indicate that it is stable throughout the whole pressure range of the upper mantle (Knittle et al. 1992). Katoite, instead, undergoes phase transitions under increasing pressure. Single-crystal X-ray diffraction (XRD) experiments by Lager et al. (2002) suggested a possible phase transition from $Ia\bar{3}d$ to $I\bar{4}3d$ symmetry, at about 5 GPa. A recent theoretical investigation by Erba et al. (2015) supported the thermodynamical instability of the $Ia\bar{3}d$ phase above 5 GPa, but found the $I\bar{4}3d$ phase to be stable only above 15 GPa; in the $5-15$ GPa range both phases were described as unstable. O'Neill et al. (1993) investigated the elastic properties of natural hibschite hydrated to 42% and observed a compressibility about 40% higher than that of anhydrous grossular. An explanation was proposed, relying on the larger volume of the $[H_4O_4]^{4-}$ tetrahedron compared with the smaller, more rigid $[SiO_4]^{4-}$ tetrahedron. By comparing isothermal densities calculated at 300 K for two chemically equivalent assemblages, one containing hibschite and the other containing grossular plus H_2O as separated phases, they found the former to be denser (and therefore thermodynamically more stable) within the pressure range of the Earth's upper mantle.

Natural occurrences of hydrogrossular, along with laboratory syntheses carried out at high temperatures (> 420 K) and pressures, suggest the existence of a continuous solid solution between the two end-members: grossular ($x = 0$) and Si-free katoite ($x = 3$). Numerous phases, scattered throughout the compositional range, were synthesized via hydrothermal treatment (Cheng et al. 1990, Cohen-Addad et al. 1967, Flint et al. 1941, Geiger et al. 2012, Lager et al. 1989). However, Jappy and Glasser (1991) showed that the mutual solubility of the end-members changes significantly at lower temperatures and pressures. Investigating

stability and solubility of solid solutions synthesized in the katoite range of composition at $370\,\mathrm{K}$ and 10^{-4} GPa pressure, they found a miscibility gap between compositions $Ca_3Al_2(SiO_4)_{0.42}(H_4O_4)_{2.58}$ and $Ca_3Al_2(SiO_4)_{0.76}(H_4O_4)_{2.24}$, and a maximum Si content attainable of $Ca_3Al_2(SiO_4)_{0.99}(H_4O_4)_{2.01}$. Results consistent with the existence of a miscibility gap occurred also in later works (Bennett et al. 1992, Dilnesa et al. 2014, Kyritsis et al. 2009). This indicates that hydrogrossular is a non-ideal solid solution.

In the present study, structural and energetic properties of the hydrogrossular series are investigated with *ab initio* simulations. The composition range from 0% to 100% grossular is explored, with reference to the 12 tetrahedral sites available for substitution in the end-member primitive cell. This allows for explicitly considering compositions $x = 0, 0.25, 0.5, 0.75, 1, 1.25, 1.5, 1.75, 2, 2.25, 2.5, 2.75, 3$. Each intermediate term is represented by a number of independent atomic configurations that were efficiently selected via symmetry-adapted Monte-Carlo (SA-MC) sampling, as recently proposed by Mustapha et al. (2013) and D'Arco et al. (2013). For all configurations, minimum energy structures have been calculated at the B3LYP level of theory, using all-electron Gaussian-type basis sets. Both SA-MC and geometry optimizations have been performed with the quantum-chemistry software package for periodic calculations CRYSTAL14 (Dovesi et al. 2014a,b). The same computational setup has already been successfully applied for studying structural, energetic, spectroscopic, elastic and optical properties of the end-members grossular and Si-free katoite (Erba et al. 2014a,b, 2015, Mahmoud et al. 2014, Orlando et al. 2006, Pascale et al. 2004), and of the grossular-andradite joint (De La Pierre et al. 2013, Lacivita et al. 2013, 2014).

The results presented in the following provide new outlook on the relationship between excess mixing enthalpy and volume of the hydrogrossular solid solution. This is important information to accomplish production of densely packed and pressure-resistant concretes. In the same vein, one can infer valuable clues about the compositions that would be most favored under the pressure of the Earth's mantle. Finally, some of the results can also be interesting to other minerals showing hydrogarnet-type substitutions, such as crystalline zircon $ZrSiO_4$ (Balan et al. 2013, Botis et al. 2013).

THEORETICAL METHOD

Structural Model for Solid Solutions

Garnet end-members have a cubic structure of space group $G \equiv Ia\bar{3}d$, with $|G| = 48$

symmetry operators. Reference is here made to the primitive unit cell of grossular (Gro), which contains 80 atoms and counts 4 formula units. The structure displays dodecahedral (Ca), octahedral (Al) and tetrahedral (Si) crystallographic sites. There are 12 tetrahedral sites available for hydrogarnet substitution, $Si^{4+} \leftrightarrow 4H^{+}$. Solid solutions are obtained by progressively replacing Si cations with 4 protons at a time. When the number *n* of Si cations is reduced to zero, the Si-free katoite (Kat) end-member is obtained. Apart from the end-members Gro (n = 12) and Kat (n = 0), eleven intermediate compositions are explicitly considered: $n = 1, 2 \ldots 11$.

For each intermediate composition, $12!/[n!\,(12-n)!]$ substitutional atomic configurations can be defined, which sum up to 4096 over the whole range of compositions. This number can be significantly reduced following the symmetry analysis recently proposed by Mustapha et al. (2013). Configurations are naturally partitioned into symmetry-independent classes (SICs), according to the operators retained after substitution. Given H_l^n the subgroup of symmetry associated to the *l*-th class of composition *n*, the number of configurations belonging to that SIC is

$$M_l^n = \frac{|G|}{|H_l^n|} \tag{1}$$

Since all configurations of a given class are equivalent to each other, the number of calculations to be actually performed reduces to only one per SIC. M_l^n can then be interpreted as the multiplicity of class *l*. The macroscopic properties of the solid solution are calculated as Boltzmann averages over all SICs, where every class weighs in proportion to its own multiplicity M_l^n. For example, the average volume is defined as

$$\bar{V}(n) = \sum_l P_l^n V_l^n \tag{2}$$

where the sum runs over the SICs of composition *n* and

$$P_l^n = \frac{M_l^n \mathrm{e}^{-\frac{\Delta E_l^n}{k_b T}}}{\sum_l M_l^n \mathrm{e}^{-\frac{\Delta E_l^n}{k_b T}}} \tag{3}$$

is the probability of finding the *l*-th SIC at temperature T. $\Delta E_l^n = E_l^n - E_{min}^n$ is the difference between its energy E_l^n, and the energy of the most stable configuration with the same chemical composition, E_{min}^n.

For the present system, a total number of 136 SICs is expected on the basis of Pòlyà's theorem (Pòlyà and Read 1987). These SICs are distributed over the composition range as outlined in Table I. Depending on the number n of Si atoms in the primitive cell, fractional composition $x = 3(1 - n/12)$, number of SICs N_{SIC}, total number of atomic configurations N_{Conf} and minimum multiplicity M_{min} (corresponding to the maximum symmetry) of the respective classes are reported. At each composition, canonical representatives for the various SICs have been selected via uniform at random SA-MC sampling, as recently devised by D'Arco et al. (2013) and implemented in the CRYSTAL14 code (Dovesi et al. 2014a,b). The basics of the SA-MC method are provided as supplementary information, along with a brief outline of the practical procedure adopted to build the classes of configurations. We address the reader to (D'Arco et al. 2013) for a comprehensive theoretical treatment, and to (Dovesi et al. 2014b) for details about the mentioned computational options.

A general concern about simulations of disordered crystalline materials and solid solutions is related to the size of the adopted structural model. Is it large enough? If large super-cells (multiples of the primitive one) seem preferable for comparison with real systems, one has to take into account practical feasibility aspects. The larger the super-cell, the more numerous the SICs, so as the number of calculations to be performed rapidly becomes prohibitive. It is necessary to find the right balance between accuracy and computational costs, by analyzing carefully every situation. For example, when dealing with dilute defects, large (to some extent) super-cells must be used in order to reduce the interactions between them. This is not a problem because the presence of a single defect in the cell corresponds to only one symmetry-independent configuration to be structurally optimized. Furthermore, for sufficiently low concentrations, calculations can be performed by freezing in some geometrical variables. In the case of concentrated solutions, as the ones studied in this work, no simple choice exists. The size of the unit cell must be large enough to allow access to different intermediate compositions and to account for eventual atomic clustering. In addition, one must bear in mind that the impact of the theoretical approximation might be property-dependent. As regards the average geometrical properties here calculated, we will show in the next section that a close comparison with experiments on the actual solid solution is achieved. This makes us confident on the accuracy of our results and, consequently, on the appropriateness of the model system chosen for the present work.

Computational Details

All calculations have been performed with the CRYSTAL14 program (Dovesi et al. 2014a,b). Minimum energy structures of all SICs were calculated at the B3LYP level of theory (Becke 1993), using all-electron atom-centered Gaussian-type basis sets. Oxygen, hydrogen, silicon, aluminum and calcium atoms were described by (8s)-(411sp)-(1d), (31s)-(1p), (8s)-(6311sp)-(1d), (8s)-(611sp)-(1d) and (8s)-(6511sp)-(21d) contractions of primitive functions, respectively.

In CRYSTAL14, density functional exchange-correlation contributions are evaluated by numerical integration over the cell volume: radial and angular points of the atomic grid are generated through Gauss-Legendre and Lebedev quadrature schemes. For the present calculations, an accurate predefined pruned grid was employed, corresponding to 99 radial and 1454 angular points. Hartree-Fock exchange contributions to the hybrid functional were calculated for atomic functions within a maximum distance of 59 direct lattice vectors $\vec{g}$ from the origin. The reciprocal space was sampled according to a sub-lattice with shrinking factor 3, which corresponds to a number of $\vec{k}$-points in the irreducible first Brillouin zone between 4 and 14, depending on the symmetry of the configuration. The convergence threshold on the self-consistent-field energy was set to 10^{-9} Ha.

As regards geometry optimizations, CRYSTAL14 calculates analytical energy gradients with respect to both atomic coordinates and unit-cell parameters (Civalleri et al. 2001, Doll 2001, Doll et al. 2001). A quasi-Newton optimization scheme is adopted in combination with the Broyden-Fletcher-Goldfarb-Shanno algorithm (Broyden 1970a,b, Fletcher 1970, Goldfarb 1970, Shanno 1970) for Hessian updating. Convergence is checked on the root mean square of both gradient components and nuclear displacements, the corresponding tolerances being 0.0003 a.u. and 0.0012 a.u., respectively.

RESULTS AND DISCUSSION

Lattice

As previously recalled, the end-members of the hydrogrossular series belong to the cubic space group $Ia\bar{3}d$. From a microscopic point of view, fractional occupancies of the tetrahedral sites at the intermediate compositions imply necessarily certain lowering of the local symmetry. Despite this, all 136 atomic configurations maintain a pseudo-cubic metric after geometry relaxation. Optimized structural parameters of all configurations can be found in the supplementary material. Here, for clarity sake, we explicitly discuss the case $n = 6$, that corresponds to the situation where half of the tetrahedral sites is occupied by Si^{4+} and the

other half by $4H^+$. This is the most illustrative composition as it provides the widest spectrum of symmetry-independent atomic distributions for the given number of substitutional sites. Table II reports lattice parameters a, b, c and angles α, β, γ for the representatives of the SICs proper of this composition. The SICs are listed in order of increasing energy, which varies by 51 mHa between $l = 1$ to $l = 32$. Multiplicities M and lattice types (as deduced from the residual symmetry H) of the various SICs are indicated. We notice that only one SIC out of 32 maintains the cubic symmetry of the aristotype (except for the inversion center). That is class $l = 32$, with $M = 2$. Many SICs are triclinic, i.e., with multiplicity $M = 48$ ($l = 4, 7, 10, 11, 13, 16, 17, 18, 19, 21, 25, 26, 30$). According to Eq. (1), this means they are asymmetric, the unique operator in H being the identity. Other SICs belong to monoclinic ($l = 5, 9, 12, 14, 15, 22, 23, 24, 28$), orthorhombic ($l = 1, 6, 8$), tetragonal ($l = 2, 3, 27, 29$) and trigonal ($l = 20, 31$) crystal systems, with respective multiplicities $M = 12$ or 24, $M = 12$, $M = 6$ or 12 and $M = 8$.

Despite the differences in symmetry, all SICs are rather close to the cubic metric: cell edges differ from each other by 0.203 Å at most, and the angles depart from 90° by less than 1.3°. For statistical purposes, we may refer to the percentage difference Δ with respect to the cubic average $\bar{a} = (a + b + c)/3$, or to the right angle. The average with sign, $\bar{\Delta}$, indicates that a is slightly biased towards elongation, while c tends to shorten. Apart from that, it is noteworthy that the absolute average difference, $|\bar{\Delta}|$, is maintained well below 1%, and not even the largest absolute percentage deviations, $\max|\Delta|$, come to exceed such a threshold (but for β, where a slightly larger deviation of 1.43% is found). These findings are consistent with the picture arising from experimental studies, according to which hydrogrossular essentially retains the cubic structure of the end-members (Basso et al. 1983, Cheng et al. 1990, Cohen-Addad et al. 1967, 1963, Ferro et al. 2003, Flint et al. 1941, Jappy and Glasser 1991, Lager et al. 1989, Pabst 1937, 1942, Passaglia and Rinaldi 1984, Sacerdoti and Passaglia 1985).

Excess Quantities

Excess enthalpies, ΔH, and volumes, ΔV, are obtained as differences between the calculated values and the values expected for an ideal system, i.e., a system whose properties vary linearly with the composition. ΔH and ΔV of the 136 configurations optimized along the Gro-Kat binary are shown in Figures 2 and 3, respectively. Each composition n goes with its complementary, $12 - n$, as regards number, multiplicity and symmetry of the respective

SICs (see Table I). However, the properties calculated at compositions n and $12 - n$ may be quite different, as we shall discuss below.

Enthalpy. In Figure 2, ΔH represents the free energy of mixing at 0 K. This is found to be negative for all the SICs throughout the compositional range. At compositions from $n = 2$ to $n = 10$, an energy range $[\min \Delta H(n) - \max \Delta H(n)]$ spreads between the most stable and the least stable SICs. The width of the range is quite large (≈ 30 mHa on average), oscillating within a maximum of 51 mHa at $n = 6$, and a minimum of 11 mHa at $n = 10$. Apart from $n = 3$, configurations at the extremes of the energy range always display some symmetry ($M < 48$). This is in line with a conjectured symmetry-energy relationship suggesting that the critical points of the potential energy surface should correspond to symmetric structures (Pauling 1929, Pickard and Needs 2011, Wales 1998).

For most of the compositions here explored, the minimum enthalpy configuration is far more stable than the other SICs with the same composition: the Boltzmann distribution would leave the ground state only at temperatures above 700 K. The only exceptions, in this respect, are $n = 2$ and $n = 7$, where the difference between $\min \Delta H$ and the next SIC is just 0.05 mHa (indistinguishable in Figure 2) and 0.8 mHa, respectively.

Function $\min \Delta H(n)$ is very asymmetric: it rapidly decreases upon substitution of 1 to 4 tetrahedral sites in Kat and then, as the silicon content increases further, it goes back to zero (Gro) less sharply. The global minimum is found at $n = 4$. In addition, a discontinuity is encountered between $n = 7$ and $n = 8$ that makes $n = 8$ a local minimum. The presence of two minima indicates that $\min \Delta H(n)$ is not always concave upward but rather reverses its curvature between these two points. This means that solid solutions in the range $4 < n < 8$ exhibit a higher enthalpy than a mixture of two separate phases with respective compositions $n = 4$ and $n = 8$. Outside this range, solid solutions are thermodynamically favored by the excess enthalpy. In particular, it turns out that $\min \Delta H(n)$ assists the insertion of silicon into Kat more than that of hydrogen into Gro.

Finally, we note that the global minimum at $n = 4$ corresponds to a solid solution with stoichiometry $Ca_3Al_2(SiO_4)(H_4O_4)_2$, that is the ideal formula assigned to the katoite mineral (Passaglia and Rinaldi 1984). Moreover, this is just about the upper limit observed by Jappy and Glasser (1991) for the substitution of Si into Kat at low temperature (95°C) and under ambient pressure. As regards $n = 8$, instead, the ideal composition of the hibschite mineral is matched, namely $Ca_3Al_2(SiO_4)_2H_4O_4$ (Belyankin and Petrov 1941, Pabst 1937).

Volume. The excess volume, ΔV, of the optimized SICs is represented in Figure 3. It is noteworthy that the most stable SICs at the various compositions correspond to high ΔV values, if not directly to $\max \Delta V$. In particular, the largest positive excess volume occurs at $n = 4$, being associated with the global minimum of the enthalpy of mixing. In contrast, the least stable SICs show excess volumes among the most negative ones.

At ambient temperature, $\Delta \bar{V}(n)$ describes a somehow sinusoidal pattern: it is negative for $0 < n < 3$, it becomes positive at $n = 3$, and negative again at about $n = 8$ up to $n = 12$. Positive ΔV values occur precisely between the two minima of the excess enthalpy, located at $n = 4$ and $n = 8$, namely where the concavity of the function $\min \Delta H(n)$ turns downwards. That is to say, if we had restricted our analysis to the range of composition $4 \leq n \leq 8$, we would have found a positive $\Delta H(n)$ function with respect to the extremes. In physical terms, this trend of $\Delta \bar{V}(n)$ means that the volume of mixing decreases for dilute solutions of either Gro into Kat or Kat into Gro, and conversely increases for solid solutions of intermediate compositions ($4 \leq n < 8$). As a consequence, in this intermediate range, the solubility is expected to reduce with increasing pressure.

Figure 4 (upper panel) shows the variation of the average volume $\bar{V}$ along the Gro-Kat binary. The relevant information available in the literature is rich but quite heterogeneous. For the sake of comparison, we have selected a set of experimental data as consistent as possible. Solid solutions with significant amounts of impurities - mostly Fe^{3+}, or with a sum of the stoichiometric fractions of Si and $\frac{1}{4}$H very different from 3, have been excluded. These include the synthetic terms 2-10, 13, 14 and 15-19 from the work of Flint et al. (1941). Synthetic samples by Jappy and Glasser (1991) with $x \leq 2$ were discarded as well, relying on the authors' distrust for contamination by $CaO - SiO_2 - H_2O$ gel phase. We also omitted "jade" samples (Frankel 1959, Tilley 1957) given the questionable reliability of their chemical analyses (Zabinski 1966).

As regards the end-members (empty squares), we considered the average of the volumes measured by Cohen-Addad et al. (1963) and Lager et al. (1987a, 2002, 2005) for Kat; by Flint et al. (1941), Novak and Gibbs (1971), Lager et al. (1987b), Olijnyk et al. (1991), and Rode- horst et al. (2002) for Gro. Note that the linear sum of these volumes (solid red line) is perfectly parallel to the ideal trend obtained from our calculations (solid black line). Besides, a slight overestimation of the experimental data (about 2.5%) meets expectations on the performance of the B3LYP functional (Paier et al. 2007).

Natural katoite is rather rare. Passaglia and Rinaldi (1984) resolved a cubic structure of

space group $Ia\bar{3}d$ and cell parameter $a = 12.358$ Å (empty triangle), while later refinements by Sacerdoti and Passaglia (1985) yielded $a = 12.379$ Å (full inverted triangle). Ferro et al. (2003) described a new sample with cubic cell parameter $a = 12.286$ Å (full pentagon). We notice that both natural katoite samples display stoichiometry close to $Ca_3Al_2SiO_4(H_4O_4)_2$, which corresponds to the global minimum of the excess enthalpy here estimated at $n = 4$. This evidence further supports the thermodynamic stability of this composition. Figure 4 also reports volume values of some synthetic katoite samples: i) empty circles represent the hydrothermal members number 1 and 12 from Flint et al. (1941); ii) asterisks are samples by Jappy and Glasser (1991); iii) empty rhombi are taken from Pöllmann (2012). By inspection of the lower panel of Figure 4, it turns out that most of the above mentioned katoite samples display a negative excess volume. The only exceptions are the synthetic specimens from Pöllmann (2012), plus two other synthetic samples (Flint et al. 1941, Jappy and Glasser 1991) of composition very close to the pure Si-free compound.

The three data points around $n = 7$ correspond to different experiments carried out on hibschite from Crestmore. Powder XRD analyses by Pabst (1937) provided a cubic structure with lattice constant $a = 12.16$ Å (solid rhombus). Afterwards, hibschite was subjected to single-crystal XRD by Basso et al. (1983), who obtained a lattice constant $a = 12.174$ Å (solid triangle). The authors relied on the chemical formula calculated from the structure refinement, namely $Ca_3Al_2(SiO_4)_{1.53}(H_4O_4)_{1.47}$, despite their own microprobe analysis revealing a distinctly higher Si content: $Ca_{2.98}Mg_{0.05}Fe_{0.02}Al_{1.93}(SiO_4)_{1.77}(H_4O_4)_{1.23}$. Indeed, in view of the remarkable agreement with the composition previously obtained by Pabst (1942), $Ca_{3.01}Al_{2.11}(SiO_4)_{1.82}(H_4O_4)_{1.10}$, we assumed their microprobe analysis as the most representative. This choice is in line with the outcome of an independent electron microprobe analysis performed by O'Neill et al. (1993), which provided chemical composition $Ca_{2.84}Mg_{0.04}Fe_{0.03}Al_{1.87}(SiO_4)_{1.72}(H_4O_4)_{1.28}$. The corresponding lattice parameter, $a = 12.183$ Å (solid square), was measured via single-crystal XRD. It is noteworthy that all the experiments performed on hibschite from Crestmore provide a positive excess volume $\Delta\bar{V}$.

Members in the range $8 \leq n \leq 12$ were synthesized by Cohen-Addad et al. (1967) (cross), by Lager et al. (1989) (plus), and by Cheng et al. (1990) (solid circles). The empty rhombus belongs to the set of synthetic hydrogrossular samples reported by Pöllmann (2012). All these points occur below the solid red line joining the two end-members. In particular, Cheng et al. (1990) carried out a thorough XRD and XPS (X-ray photoelectron spectroscopy)

investigation in order to define a quantitative relation between unit cell dimension and composition $0 \leq x \leq 1$. They found it to be nonlinear, with a negative volume of mixing describing an asymmetric pattern.

Let us focus now on the lower panel of Figure 4. We notice that the collection of experimental excess volumes suggests a sinusoidal trend of the function $\Delta\bar{V}$, which is qualitatively very similar to that described by our calculated data. Indeed, $\Delta\bar{V}$ is generally negative for Kat-rich solid solutions (n up to $4-5$), it is positive at intermediate compositions ($n \approx 7$), and finally returns negative for Gro-rich solid solutions ($8 \leq n < 12$). The agreement between experimental and calculated data is satisfactory, apart from the latter suffering from a slight underestimation of the amplitude of the negative $\Delta\bar{V}$ values. On the hibschite side, the intersection with the zero axis occurs around $n = 8$ in both series. On the katoite side, instead, the present calculations seem somehow to anticipate (at $n = 3$) the sign reversal of $\Delta\bar{V}$ with respect to the experiments (about $n = 4 - 5$). Nevertheless, it is also true that the measurements on katoite are rather dispersed in comparison with those on hibschite. At intermediate compositions ($4 < n < 8$) we cannot compare precisely, because the available experimental data are scarce, and because those on hibschite from Crestmore are located right at the discontinuity of the calculated functions $\Delta\bar{V}(n)$ and $\Delta\bar{H}(n)$. We may just remark that samples reported by Pöllmann (2012) with positive excess volume lie very close to the corresponding calculated points.

Octahedra

Figure 5 shows the variation of the octahedral-dodecahedral shared, S, and unshared, U, edges with composition. The shared edge S is represented in the upper panel. We notice that the three oxygen pairs are well distinguished, being always $S(\mathrm{OH}-\mathrm{OH}) < S(\mathrm{O}-\mathrm{OH}) < S(\mathrm{O}-\mathrm{O})$. All three distances are shortened with the increase of the number n of Si atoms in the primitive cell. Apart from the end-members Gro and Kat, hetero-pairs $\mathrm{O}-\mathrm{OH}$ are present along the entire compositional range. In contrast, the distribution of homo-pairs, $\mathrm{OH}-\mathrm{OH}$ and $\mathrm{O}-\mathrm{O}$, is very asymmetrical: compositions with $n < 5$ are characterized by the exclusive presence of $\mathrm{OH}-\mathrm{OH}$ pairs, while those with $n > 7$ display only pairs of type $\mathrm{O}-\mathrm{O}$. This may be related to the corresponding asymmetry of the excess enthalpy (Figure 2), so that the simultaneous presence of $\mathrm{OH}-\mathrm{OH}$, $\mathrm{O}-\mathrm{OH}$ and $\mathrm{O}-\mathrm{O}$ shared edges, occurring just between $n = 5$ and $n = 7$, may be related to the concavity change of the excess enthalpy in the same range of compositions. By plotting the weighted average $\bar{S}$ with increasing n, we get an

upward linear (within the stripe width) trend that would indicate the elongation of the shared edge with the increase of Si atoms. In fact, despite the shortening of S for each oxygen pair type, the progressive increase in weight of the $O-O$ pair determines the increase of $\bar{S}$. This result is in perfect agreement with the average structure view provided by experimental determinations (red asterisks).

As regards the unshared edge U (lower panel), the lengths associated to pairs $OH-OH$, $O-OH$ and $O-O$ are much closer to each other. All of them slightly decrease with increasing n, with a variation of just 0.12 Å over the whole composition range. In this case, the average function $\overline{U}$ is consistent with the individual trends: it provides a linear (within the stripe width) shortening of the unshared edge with an increasing number of Si atoms. Again, the predicted average behavior conforms to the experiments (red asterisks).

To recap, average $\bar{S}$ and $\overline{U}$ octahedral edge lengths are consistent with a macroscopic picture according to which the shared octahedral edge decreases in length while the unshared edge increases. They intersect at about $n = 10$ (vertical dashed line in Figure 5), that is very close to the crossing between the experimental curves (Lager et al. 1989).

Tetrahedra Distribution and Structural Response to Hydrogarnet Substitution

From the discussion addressed above (Section IIIB), one may deduce that, within the present model, the Gro-Kat solid solution at low temperature can essentially be represented by the most stable configurations at the various compositions. Therefore, unless otherwise stated, the following structure analysis will refer to configurations of minimal enthalpy (red points in Figure 2). In order to rationalize the effects of the hydrogarnet substitution, we will exploit the typical polyhedral interpretation of the garnet structure (Novak and Gibbs 1971). That is, hydrogrossular consists of a three-dimensional network of alternating, corner-sharing SiO_4 (or H_4O_4) tetrahedra and AlO_6 octahedra, in which triangular dodecahedral cavities accommodate Ca^{2+} cations.

Oxygens and Hydroxyls. Figure 6 shows $\delta-O$ distances between the barycenter δ of the tetrahedra and the O atoms at their vertices, as a function of the composition. It turns out that both kinds of tetrahedra are rather insensitive to variations in composition, more so for the SiO_4 tetrahedra, where the presence of a central Si atom freezes the oxygens via covalent interactions. Protonated H_4O_4 tetrahedra lack such an internal constraint and thus display a wider dispersion of the $\delta-O$ distances. To get a quantitative estimation of the tetrahedral distortion at intermediate compositions, we applied the iterative least-squares technique

454 proposed by Dollase (1974), and obtained maximum deformations of 4.5% for SiO_4
455 compared to Gro, and 5.2% for H_4O_4 compared to Kat. These deformation rates are rather
456 low, which indicates both the tetrahedral sites to be fairly close to the respective "ideal" limit
457 structures.

458 According to our calculations, the oxygens of the solid solution are unambiguously split
459 into Gro-like and Kat-like tetrahedral sites, whatever the composition. This picture is
460 consistent with experimental refinements by Armbruster and Lager (1989) and by Lager et al.
461 (1989), who successfully adopted the split-atom model to account for oxygen positional
462 disorder in katoite and hibschite samples, i.e., oxygen sets on two different sites depending
463 upon whether the tetrahedron is occupied by Si or protonated. They worked out, in this way,
464 anomalously short $O-H(D)$ bond distances ($0.65-0.74$ Å) previously reported (Lager et
465 al. 1987a, 1989, Sacerdoti and Passaglia 1985), as artifacts due to the use of standard ordered
466 refinement models yielding a single average oxygen position rather than the two real ones.

467 In fact, by considering a weighted mean of the calculated $\delta-O$ values for SiO_4 and
468 H_4O_4tetrahedra, a linear function of composition is obtained (gray stripe in Figure 6), which
469 decreases from 1.979 Å at $n=0$ (Kat), to 1.662 Å at $n=12$ (Gro). This coincides with the
470 average picture provided by XRD experiments (red asterisks).

471 **Hydrogen interactions.** Let us now analyze what happens to the hydrogen atoms. We are
472 interested in investigating the possible existence and/or development of hydrogen interactions
473 along the compositional series. In the absence of vibrational data on which to rely for
474 evaluating presence and strength of possible H-bonds, we must refer to geometric criteria. As
475 a guideline on the structural systematics of hydrogen bonding in inorganic compounds, we
476 used the accurate compilations provided by Ceccarelli et al. (1981) and by Nyfeler and
477 Armbruster (1998). Based on these works, one can deduce that the average $O-H$ distance
478 generally settles around 0.969 Å, the $H\cdots O$ bond lengths range within $1.75-1.82$ Å and
479 the average $O-H\cdots O$ angle is about 167°. Given the broad structural variety of crystalline
480 solids, these values cannot be considered as real cutoffs, but rather as references for hydrogen
481 interactions of significant strength: the further away from this model geometry, the weaker (if
482 any) the interaction.

483 We may start considering the H_4O_4tetrahedron in Kat ($n=0$). The optimized structure
484 obtained in the present work compares well with experimental determinations. A distance
485 $\delta-O$ of 1.979 Å is calculated, which is quite similar to both neutron and X-ray diffraction
486 measurements, i.e., 1.950 Å and 1.962 Å, respectively (Lager et al. 1987a). Hydrogens are

located slightly outside the tetrahedron, the angle $\delta - O - H$ being 36°. Our computed $O - H$ bond length, i.e., 0.961 Å, is in line with previous calculations (Pascale et al. 2004) as well as with targeted structure refinements corrected for thermal motion effects, i.e., 0.95 Å (Lager et al. 2005). According to Lager et al. (2005) a bifurcated H-bond is formed with the oxygens located at the opposite vertices of the face, with the H atom lying approximately on the bisector plane. They collected time-of-flight neutron powder data on $Ca_3Al_2(D_4O_4)_3$, measuring two intra-tetrahedral $D \cdots O$ distances, $D1 \cdots O3 = 2.551$ Å and $D1 \cdots O3' = 2.499$ Å (notation as in Figure 7), and respective angles $O1 - D1 \cdots O3 = 133.5°$ and $O1 - D1 \cdots O3' = 139.6°$. In addition, they identified an inter-tetrahedral H-bond, $D3 \cdots O1'$, as large as 2.606 Å, with an angle $O3 - D3 \cdots O1'$ equal to 111.1°.† A clear divergence from the geometric H-bond requirements here adopted (Ceccarelli et al. 1981, Nyfeler and Armbruster 1998) is observed, which implies at least the classification into rather weak interactions. That said, our calculations define pretty much the same picture: i) the intra-tetrahedral parameters are $H1 \cdots O3 = 2.564$ Å, $H1 \cdots O3' = 2.513$ Å, $O1 - H1 \cdots O3 = 133.2°$ and $O1 - H1 \cdots O3' = 138.8°$; ii) the inter-tetrahedral parameters are $H3 \cdots O1' = 2.610$ Å and $O3 - H3 \cdots O1' = 109°$. These values are reported in Table III and compared with selected distances and angles of minimum energy SICs calculated at different compositions n.

When a silicon atom is introduced in the unit cell ($n = 1$), one H_4O_4 tetrahedron is replaced for SiO_4. This causes a drastic change in the geometry of the hydrogen interactions in the neighborhood. We focus on the first star of neighbors, i.e., four H_4O_4tetrahedra on which the perturbation is evenly distributed as each of them interacts with one oxygen of the SiO_4unit. Figure 7 shows the detail of the local rearrangement. H3 flips toward O1′ with a dramatic enlargement of the angle $\delta - O3 - H3$ ($65.5°$). The simultaneous gain in directionality of the inter-tetrahedral interaction ($O3 - H3 \cdots O1' = 148.7°$) implies a strengthening of the latter, that is deduced from the increment of the $O3 - H3$ bond length (0.969 Å) and from the corresponding decrease of the $H3 \cdots O1'$ distance (2.077 Å). Meanwhile, the repulsion exerted by H3 on the other three hydrogens of the H_4O_4 tetrahedron fades, so that they can come closer to its center δ. H1 is particularly concerned: the angle δ-O1-H1 tightens to 24.21°, and the intra-tetrahedral interaction with O3 intensifies

†We recall that, in cubic Si-free katoite, oxygen atoms, as well as hydrogen atoms, are all equivalent. The proposed labeling is a convenient way to discuss geometrical relations.

517 ($H1 \cdots O3 = 2.335$ Å, $O1 - H1 \cdots O3' = 148.0°$) at the expense of the one with $O3'$
518 ($H1 \cdots O3' = 2.593$ Å, $O1 - H1 \cdots O3' = 134.4°$). This suggests that the position of the H
519 atoms is controlled by the electrostatic interactions between them, rather than by hydrogen
520 interactions, and thus emphasizes the weakness of the latter.

521 In the opposite situation, that is when all tetrahedra but one are occupied by Si ($n = 11$),
522 we obtain a fairly different arrangement of the hydrogen atoms (see Table III). This time, a
523 single H_4O_4 tetrahedron is surrounded by four SiO_4 tetrahedra. Each hydrogen of H_4O_4
524 interacts with one SiO_4 tetrahedron at a distance $H3 \cdots O1'$ of 2.191 Å, forming angles
525 $O3 - H3 \cdots O1' = 127.1^{\circ}$ and $\delta - O3 - H3 = 45.52^{\circ}$. By comparison with $n = 1$, we can
526 infer that hydrogen interactions in this case are generally not as strong. A certain asymmetry
527 emerges, which may be somehow reflected by the excess enthalpy represented in Figure 2:
528 ΔH is about -18 mHa at $n = 1$ and about -7 mHa at $n = 11$. Besides, we should not expect
529 otherwise given that the ratio of hydrogen donor-to-acceptor is necessarily different in the
530 two cases. At $n = 1$ there are four H_4O_4 tetrahedra (donors) strongly engaged in as many
531 hydrogen interactions with one SiO_4 (acceptor). The latter acts as an attractive pole for the
532 nearest hydrogen atoms, thus unbalancing the layout of the surroundings. At $n = 11$ it
533 remains a single H_4O_4 tetrahedron (donor). Its hydrogens participate one-by-one in
534 interactions with four neighboring SiO_4 tetrahedra (acceptors) that are evenly spaced out. The
535 result is an isotropic "strain" of the donor with respect to the reference Kat.

536 At intermediate compositions, hydrogen interactions are far more complicated to
537 rationalize. The parameters reported in Table III for $n = 4, 6$ suggest stronger interactions
538 than in Kat, but their input to the stability of the system is blurred by new rising
539 contributions. At $n = 6$, for instance, the most stable and the least stable SICs exhibit
540 hydrogen interactions of comparable strength, the difference being rather in their number.
541 One would expect that the higher the number of interactions, the more stable the structure. In
542 fact, we find the opposite situation: in the least stable SIC, which has cubic symmetry, each
543 tetrahedron $H_4O_4(SiO_4)$ interacts with four neighbors $SiO_4(H_4O_4)$; in the most stable SIC,
544 instead, the inter-tetrahedral hydrogen interactions are halved. Indeed, we may conclude that
545 the necessity to invoke "H-bonds" to understand the energetics of the system is not so
546 obvious. It is to be recalled that such partitioning of the energy is nothing but the result of a
547 rational process of interpretation, which can be useful to account for some properties but,
548 still, is far from being fully comprehensive.

549 **Tetrahedra Distribution.** Figure 8 shows the distribution of the H_4O_4 and SiO_4 tetrahedra
550 in the pseudo-cubic cell of minimum energy configurations at different compositions n (the
551 number of Si atoms refers to the primitive cell). Two distinct patterns of distribution can be
552 recognized: one for $n \leq 7$ and another one for $n \geq 7$ (SICs with $n \leq 3$ and $n \geq 11$ are not
553 shown in the figure as they are poorly illustrative). On the katoite side ($n < 7$), the
554 SiO_4 tetrahedra are progressively arranged in planes $(1\ 0\ 1)$, until a structure of alternate
555 "layers" of Gro and Kat is finally obtained at n = 6. Hence, a tendency emerges towards some
556 sort of separation between the two phases, which accounts for the positive excess volumes
557 calculated at $4 \leq n \leq 6$ (Figures 3 and 4). Note that the plane of growth of the SiO_4 layers
558 coincides with the mirror planes for the pseudomerohedral twins inducing ferroelastic lattice
559 strain in majorite (Heinemann et al. 1997). We may also remark that force-field calculations
560 by Becker et al. (2000) and by Becker and Pollok (2002) provided a similar tendency to
561 cation ordering in alternating layers for $1:1$ compositions of barite-celestite and grossular-
562 andradite solid solutions, respectively. On the hibschite side ($n > 7$), a mixed distribution of
563 SiO_4 and H_4O_4 tetrahedra appears to be thermodynamically favored, which nicely correlates
564 with the negative excess volumes of Figures 3 and 4. These two tetrahedra distribution
565 patterns meet at $n = 7$, that is right at the discontinuity encountered on both the calculated
566 enthalpy and volume of mixing (Figures 2 and 3). As previously discussed, composition
567 $n = 7$ features a small energy difference (about 0.8 mHa) between $\min \Delta H$ and the next SIC.
568 Figure 8 shows the corresponding structures: the most stable at the bottom and the less stable
569 at the top. The most stable configuration displays a tetrahedra arrangement consistent with
570 the hibschite pattern, while the second is consistent with the katoite pattern. Plots of $\Delta H(n)$
571 (solid lines), represent the two series of configurations with different colors. Each color
572 corresponds to a continuity region of the excess enthalpy function. This suggests that $\Delta H(n)$
573 is given by a superposition of two different curves with minima at $n = 4$ and $n = 8$,
574 respectively, that intersect at $n = 7$. In order to decipher the effective interactions that shape
575 the $\Delta H(n)$ function, a classical "J-formalism" or cluster expansion (CE) may be applied. This
576 method was adopted, for example, by Becker and Pollok (2002) to fit the energies of mixing
577 of grossular-andradite solid solutions. In that case, the authors used a CE of pairwise cation
578 interactions only, up to third nearest neighbors. However, for a non-regular system like the
579 grossular-katoite binary, one should either extend the CE to at least three body interactions,
580 or consider pairwise interactions as functions of composition (Vinograd et al. 2010). The
581 application of such approach would be an interesting follow-up to this study.

Let us now have an insight on the tetrahedra distribution of the enthalpy local minimum at $n = 8$, which corresponds to stoichiometry $Ca_3Al_2(SiO_4)_2(H_4O_4)$. Figure 9 shows a perfect correspondence with the experimental structure of henritermierite (Armbruster et al. 2001), that is another mineral of the hydrogarnet group having formula $Ca_3Mn_2(SiO_4)_2(H_4O_4)$. Even the hydrogen positions in henritermierite resemble the arrangement provided by our calculation. Due to the Jahn-Teller distortion of octahedral Mn^{3+}, henritermierite has a tetragonal lattice (space group $I4_1/acd$), with cell parameters $a = 12.489$ and $c = 11.909$ Å and a ratio $a/c = 1.049$. An Al-dominant analogue of average composition $Ca_3(Al_{0.96}Mn^{3+}_{0.68}Fe^{3+}_{0.37})(SiO_4)_2(H_4O_4)_{0.99}$, named holstamite, has also been reported with a slightly lower ratio: $a/c = 1.034$, being $a = 12.337$ Å and $c = 11.930$ Å (Halenius et al. 2005). Holstamite belongs to a solid solution between henritermierite and a hypothetical tetragonal end-member $Ca_3Al_2(SiO_4)_2(H_4O_4)$, which, given the absence of Mn^{3+}, should be associated to the smallest a/c ratio along the series. In fact, the most stable configuration calculated at $n = 8$ does correspond to such a hypothetical end-member: it has the exact stoichiometry, a tetragonal symmetry and a pseudo-cubic unit cell with ratio $a/c = 1.023$.

IMPLICATIONS

An *ab initio* quantum-mechanical approach has been adopted to analyze structure and energetics aspects of the grossular-katoite solid solution. Calculations have been performed within the primitive cell of cubic garnets, using all-electron Gaussian basis sets and the B3LYP hybrid functional. The results obtained at the present level of approximation can be summarized as follows: i) all the 136 SICs obtained by hydrogarnet substitution feature pseudo-cubic conventional cells after full geometry relaxation; ii) at low temperatures (approximately below 700 K), the properties of the system pertain essentially to the ground state; iii) the excess enthalpy describes an asymmetric function, with two minima that can be associated to natural minerals of stoichiometry $Ca_3Al_2SiO_4(H_4O_4)_2$ and $Ca_3Al_2(SiO_4)_2H_4O_4$, respectively; iv) the asymmetry of the enthalpy of mixing can be related to two different distribution patterns of the tetrahedra H_4O_4 and SiO_4, which intersect around composition $Ca_3Al_2(SiO_4)_{1.75}(H_4O_4)_{1.25}$ ($n = 7$); v) for lower amounts of grossular, the SiO_4 tetrahedra tend to cluster in (1 0 1) planes and, consequently, the excess volume becomes positive within the range $1 \leq x \leq 1.5$; vi) hydrogen interactions also contribute to the asymmetry of the excess enthalpy as those developed around one SiO_4 in katoite ($n = 1$) are stronger than those around one H_4O_4 in grossular ($n = 11$); vii) the oxygens are unambiguously split into

614 grossular-like and katoite-like tetrahedral sites, whatever the composition; viii) hydrogen
615 interactions in fully-hydrated katoite are found to be weak as suggested by dramatic changes
616 in the H environment associated with the introduction of SiO_4 tetrahedra.

617 Implications of this work can be envisaged at different levels. The immediate fallout is
618 represented by the complement of knowledge and by the interpretive support that theoretical
619 data provide to the experimental evidence. The atomistic approach of the simulation allowed
620 us to deepen the structural analysis of hydrogrossular, establishing interesting correlations
621 with the enthalpy of the solid solution. In fact, we have shown that the hydrogarnet
622 substitution is driven by a strong enthalpy gain. All compositions are possible on the basis of
623 the calculated excess enthalpy, meaning that the reported miscibility gap between
624 compositions $Ca_3Al_2(SiO_4)_{0.42}(H_4O_4)_{2.58}$ and $Ca_3Al_2(SiO_4)_{0.76}(H_4O_4)_{2.24}$ can be filled by
625 varying temperature and pressure conditions. On a practical level, the relationship between
626 stability and excess volume of hydrogrossular can serve the purpose of controlling the
627 rheology of cement pastes and producing dense concrete structures. Also, the positive excess
628 volumes calculated for $1 \leq x \leq 1.5$ indicate that solid solutions with these compositions are
629 impeded by high pressures. The next step would be performing frequency calculations on the
630 optimized structures in order to access entropic contributions to the thermodynamics of the
631 system.

632 Besides that, the present work may also have a strong methodology impact in the field of
633 the theoretical study of solid solutions (and disordered crystals). In this regard, we have
634 shown the SA-MC sampling of the configurational space as a valuable route to tackle these
635 kinds of systems via first-principle simulations, and thus get accurate estimates of their
636 average structure and energetic properties. We can expect that the same holds true for other
637 properties (e.g., spectroscopic, dielectric, magnetic), but care must be taken when dealing
638 with tensor quantities because Boltzmann averages are not straightforward. Further work is
639 required in order to define an appropriate method for processing the calculated data in such
640 cases. Finally, there are some issues that still remain open, for example understanding the
641 relationship between symmetry and stability of the classes of configurations. We have found
642 that minima and maxima of the calculated enthalpy of mixing correspond to symmetric
643 configurations. If proven in general, this connection would be of great help in exploring
644 configurational spaces, as it would bridge directly towards minima and maxima of the
645 potential energy surface. The advantages, in terms of computational efficiency, would be
646 proportional to the size of the system: the larger the unit cell, the lower the ratio between

symmetric and asymmetric classes of configurations.

ACKNOWLEDGEMENTS

This work, partially undertaken within the framework of CALSIMLAB, is supported by the public grant ANR-11-LABX-0037-01 overseen by the French National Research Agency (ANR) as part of the "Investissements d'Avenir" program (reference: ANR-11-IDEX-0004-02). It was granted access to the HPC resources of The Institute for scientific Computing and Simulation financed by Region Ile de France and the project Equip@Meso (reference ANR-10-EQPX-29-01). We also acknowledge PRACE for awarding us access to the high-performance computing resource Hornet based in Germany at HLRS (Proposal 2014102294). Finally, we express special thanks to the anonymous referees for thoroughly reading the manuscript and providing sound comments.

660 Ackermann, L., Cemic, L., and Langer, K. (1983) Hydrogarnet substitution in pyrope: a
661 possible location for "water" in the mantle. Earth Planet Science Letters, 62, 208 – 214.
662 Aines, R.D., and Rossman, G.R. (1984) The hydrous component in garnets; pyralspites.
663 American Mineralogist, 69, 1116–1126.
664 Armbruster, T., Kohler, T., Libowitzky, E., Friedrich, A., Miletich, R., Kunz, M.,
665 Medenbach, O., and Gutzmer, J. (2001) Structure, compressibility, hydrogen bonding, and
666 dehydration of the tetragonal Mn^{3+} hydrogarnet, henritermierite. American Mineralogist,
667 86, 147–158.
668 Armbruster, T., and Lager, G.A. (1989) Oxygen disorder and the hydrogen position in garnet-
669 hydrogarnet solid solutions. European Journal of Mineralogy, 1, 363–370.
670 Atkins, M., Bennett, D.G., Dawes, A.C., Glasser, F.P., Kindness, A., and Read, D. (1992) A
671 thermodynamic model for blended cements. Cement and Concrete research, 22, 497–502.
672 Atkins, M., and Glasser, F.P. (1992) Application of portland cement-based materials to
673 radioactive waste immobilization. Waste Management, 12, 105 – 131.
674 Balan, E., Yi, H., and Blanchard, M. (2013) First-principles study of OH defects in zircon.
675 Physics and Chemistry of Minerals, 40, 547–554.
676 Basso, R., Della Giusta, A., and Zefiro, L. (1983) Crystal structure refinement of plazolite: a
677 highly hydrated natural hydrogrossular. Neues Jahrbuch Fur Mineralogie-Monatshefte, pp.
678 251–258.
679 Becke, A.D. (1993) Density-functional thermochemistry. III. The role of exact exchange.
680 Journal of Chemical Physics, 98, 5648.
681 Becker, U., Fernandez-Gonzalez, A., Prieto, M., Harrison, R., and Putnis, A. (2000) Direct
682 calculation of thermodynamic properties of the barite/celestite solid solution from
683 molecular principles. Physics and Chemistry of Minerals, 27, 291–300.
684 Becker, U., and Pollok, K. (2002) Molecular simulations of interfacial and thermodynamic
685 mixing properties of grossular-andradite garnets. Physics and Chemistry of Minerals, 29,
686 52–64.
687 Belyankin, D.S., and Petrov, V.P. (1941) The grossularoid group (hibschite, plazolite).
688 American Mineralogist, 26, 450–453.
689 Bennett, D.G., Read, D., Atkins, M., and Glasser, F.P. (1992) A thermodynamic model for
690 blended cements. II: Cement hydrate phases; thermodynamic values and modelling
691 studies. Journal of Nuclear Materials, 190, 315–325.
692 Botis, S.M., Pan, Y., and Ewing, R.C. (2013) Hydrogen incorporation in crystalline zircon:
693 Insight from ab initio calculations. American Mineralogist, 98, 745–751.

Broyden, C.G. (1970a) The convergence of a class of double-rank minimization algorithms 1. general considerations. IMA Journal of Applied Mathematics, 6, 76–90.

Broyden, C.G. (1970b) The convergence of a class of double-rank minimization algorithms 2. The new algorithm. IMA Journal of Applied Mathematics, 6, 222–231.

Ceccarelli, C., Jeffrey, G., and Taylor, R. (1981) A survey of O-H···O hydrogen bond geometries determined by neutron diffraction. Journal of Molecular Structure, 70, 255 – 271.

Cheng, W., Greenwood, H.J., Hu, H., and Frost, D.C. (1990) XRD and XPS analyses of the grossular-hydrogrossular series. Canadian Mineralogist, 28, 87–91.

Civalleri, B., D'Arco, Ph., Orlando, R., Saunders, V.R., and Dovesi, R. (2001) Hartree-Fock geometry optimisation of periodic systems with the CRYSTAL code. Chemical Physics Letters, 348, 131–138.

Cohen-Addad, C., Ducros, P., and Bertaut, E.F. (1967) Étude de la substitution du groupement SiO_4 par $(OH)_4$ dans les composés $Al_2Ca_3(OH)_{12}$ et $Al_2Ca_3(SiO_4)_{2.16}(OH)_{3.36}$ de type Grenat. Acta Crystallographica, 23, 220–230.

Cohen-Addad, C., Ducros, P., Durif-Varambon, A., Bertaut, E.F., and Delapalme, A. (1963) Étude de la position des atomes d'hydrogène dans l'hydrogrenat $Al_2O_3, 3CaO, 6H_2O$. Solid State Communications, 1, 85 – 87.

Cornu, F. (1906) XIII. Beiträge zur Petrographie des Böhmischen Mittelgebirges. Tschermaks mineralogische und petrographische Mitteilungen, 25, 249–268.

D'Arco, Ph., Mustapha, S., Ferrabone, M., Noël, Y., De La Pierre, M., and Dovesi, R. (2013) Symmetry and random sampling of symmetry independent configurations for the simulation of disordered solids. Journal of Physics: Condensed Matter, 25, 355401.

De La Pierre, M., Noël, Y., Mustapha, S., Meyer, A., D'Arco, Ph., and Dovesi, R. (2013) The in- frared vibrational spectrum of andradite-grossular solid solutions. A quantum-mechanical simulation. American Mineralogist, 98, 966–976.

Dilnesa, B.Z., Lothenbach, B., Renaudin, G., Wichser, A., and Kulik, D. (2014) Synthesis and characterization of hydrogarnet $Ca_3(Al_xFe_{1-x})_2(SiO_4)_y(OH)_{4(3-y)}$. Cement and Concrete research, 59, 96–111.

Doll, K. (2001) Implementation of analytical Hartree-Fock gradients for periodic systems. Computer Physics Communications, 137, 74–88.

Doll, K., Saunders, V.R., and Harrison, N.M. (2001) Analytical Hartree-Fock gradients for periodic systems. International Journal of Quantum Chemistry, 82, 1–13.

Dollase, W.A. (1974) A method of determining the distortion of coordination polyhedra. Acta Crystallographica, 30, 513–517.

Dovesi, R., Orlando, R., Erba, A., Zicovich-Wilson, C.M., Civalleri, B., Casassa, S., Maschio, L., Ferrabone, M., De La Pierre, M., D'Arco, Ph., Noël, Y., Causà, M., Rérat, M., and Kirtman, B. (2014a) CRYSTAL14: A program for the ab initio investigation of crystalline solids. International Journal of Quantum Chemistry, 114, 1287–1317.

Dovesi, R., Saunders, V.R., Roetti, C., Orlando, R., Zicovich-Wilson, C.M., Pascale, F., Doll, K., Harrison, N.M., Civalleri, B., Bush, I.J., D'Arco, Ph., Llunell, M., Causà, M., and Noël, Y. (2014b) CRYSTAL14 User's Manual. Università di Torino, Torino.

Erba, A., Mahmoud, A., Belmonte, D., and Dovesi, R. (2014a) High Pressure Elastic Properties of Minerals from Ab initio Simulations: The Case of Pyrope, Grossular and Andradite Silicate Garnets. Journal of Chemical Physics, 140, 124703.

Erba, A., Mahmoud, A., Orlando, R., and Dovesi, R. (2014b) Elastic Properties of Six Silicate Garnet End-members from Accurate Ab initio Simulations. Physics and Chemistry of Minerals, 41, 151–160.

Erba, A., Navarrete-López, A.M., Lacivita, V., D'Arco, P., and Zicovich-Wilson, C.M. (2015) Katoite under Pressure: An Ab initio Investigation of its Structural, Elastic and Vibrational Properties Sheds Light on the Phase Transition. Physical Chemistry Chemical Physics, 17, 2660–2669.

Ferro, O., Galli, E., Papp, G., Quartieri, S., Szakáll, S., and Vezzalini, G. (2003) A new occurrence of katoite and re-examination of the hydrogrossular group. European Journal of Mineralogy, 15, 419–426.

Fletcher, R. (1970) A new approach to variable metric algorithms. Computer Journal, 13, 317–322.

Flint, E.P., McMurdie, H.F., and Wells, L.S. (1941) Hydrothermal and X-ray studies of the garnet-hydrogarnet series and the relationship of the series to hydration products of Portland. Journal of research of the National Bureau of Standards, 26, 13–34. RP1355.

Flint, E.P., and Wells, L.S. (1941) Relationship of the garnet-hydrogarnet series to the sulfate resistance of Portland cements. Journal of research of the National Bureau of Standards, 26,13–33.

Foreman Jr., D.W. (1968) Neutron and X-Ray Diffraction Study of $Ca_3Al_2(O_4D_4)_3$, a Garnetoid. Journal of Chemical Physics, 48, 3037–3041.

Foshag, W.F. (1920) Plazolite, a new mineral. American Mineralogist, 5, 183–185.

Frankel, J.J. (1959) Uvarovite garnet and South African jade (hydrogrossular) from the

Bushveld complex, Transvaal. American Mineralogist, 44, 565–591.

Geiger, C.A., Dachs, E., and Benisek, A. (2012) Thermodynamic behavior and properties of katoite (hydrogrossular): A calorimetric study. American Mineralogist, 97, 1252–1255.

Geiger, C.A., Langer, K., Bell, D.R., Rossman, G.R., and Winkler, B. (1991) The hydroxide component in synthetic pyrope. American Mineralogist, 76, 49–59.

Goldfarb, D. (1970) A family of variable-metric methods derived by variational means. Mathematics of Computation, 24, 23–26.

Griggs, D. (1967) Hydrolytic Weakening of Quartz and Other Silicates. Geophysical Journal of the Royal Astronomical Society, 14, 19–31.

Halenius, U., Haüssermann, U., and Harrison, H. (2005) Holtstamite, $Ca_3(Al,Mn^{3+})_2(SiO_4)_{3-x}(H_4O_4)_x$, a new tetragonal hydrogarnet from Wessels Mine, South Africa. European Journal of Mineralogy, 17, 375–382.

Heinemann, S., Sharp, T.G., Seifert, F., and Rubie, D.C. (1997) The cubic-tetragonal phase transition in the system majorite ($Mg_4Si_4O_{12}$) - pyrope ($Mg_3Al_2Si_3O_{12}$), and garnet symmetry in the Earth's transition zone. Physics and Chemistry of Minerals, 24, 206–221.

Hillier, S., Lumsdon, D.G., Brydson, R., and Paterson, E. (2007) Hydrogarnet: A host phase for Cr(VI) in Chromite Ore Processing Residue (COPR) and other high pH wastes. Environmental Science & Technology, 41, 1921–1927.

Jappy, T.G., and Glasser, F.P. (1991) Synthesis and stability of silica-substituted hydrogarnet $Ca_3Al_2Si_{3-x}O_{12-4x}(OH)_{4x}$. Advances in Cement Research, 4, 1–8.

Knittle, E., Hathorne, A., Davis, M., and Williams, Q. (1992) A spectroscopic study of the high-pressure behavior of the O_4H_4 substitution in garnet, pp. 297–304. American Geophysical Union, Washington.

Kyritsis, K., Meller, N., and Hall, C. (2009) Chemistry and Morphology of Hydrogarnets Formed in Cement-Based CASH Hydroceramics Cured at 200°to 350°C. Journal of the American Ceramic Society, 92, 1105–1111.

Lacivita, V., D'Arco, Ph., Orlando, R., Dovesi, R., and Meyer, A. (2013) Anomalous birefringence in andradite-grossular solid solutions. A quantum-mechanical approach. Physics and Chemistry of Minerals, 40, 781–788.

Lacivita, V., Erba, A., Dovesi, R., and D'Arco, Ph. (2014) Elasticity of Grossular-Andradite Solid Solution: An Ab initio Investigation. Physical Chemistry Chemical Physics, 16, 15331–15338.

Lager, G.A., Armbruster, T., and Faber, J. (1987a) Neutron and X-ray diffraction study of hy-

drogarnet $Ca_3Al_2(O_4H_4)_3$. American Mineralogist, 72, 756–765.

Lager, G.A., Armbruster, T., Rotella, F.J., and Rossman, G.R. (1989) OH substitution in garnets; X-ray and neutron diffraction, infrared, and geometric-modeling studies. American Mineralogist, 74, 840–851.

Lager, G.A., Downs, R.T., Origlieri, M., and Garoutte, R. (2002) High-pressure single-crystal X- ray diffraction study of katoite hydrogarnet: Evidence for a phase transition from $Ia\bar{3}d \rightarrow I\bar{4}3d$ symmetry at 5 GPa. American Mineralogist, 87, 642–647.

Lager, G.A., Marshall, W.G., Liu, Z., and Downs, R.T. (2005) Re-examination of the hydrogarnet structure at high pressure using neutron powder diffraction and infrared spectroscopy. American Mineralogist, 90, 639–644.

Lager, G.A., Rossman, G.R., Rotella, F.J., and Schultz, A.J. (1987b) Neutron-diffraction structure of a low-water grossular at 20K. American Mineralogist, 72, 766–768.

Mackwell, S., Kohlstedt, D., and Paterson, M. (1985) The role of water in the deformation of olivine single crystals. Journal of Geophysical Research: Solid Earth, 90, 11319–11333.

Mahmoud, A., Erba, A., Doll, K., and Dovesi, R. (2014) Pressure Effect on Elastic Anisotropy of Crystals from Ab initio Simulations: The Case of Silicate Garnets. Journal of Chemical Physics, 140, 234703.

Mustapha, S., D'Arco, Ph., De La Pierre, M., Noël, Y., Ferrabone, M., and Dovesi, R. (2013) On the use of symmetry in configurational analysis for the simulation of disordered solids. Journal of Physics: Condensed Matter, 25, 105401.

Novak, G.A., and Gibbs, G.V. (1971) The crystal chemistry of silicate garnets. American Mineralogist, 56, 791–825.

Nyfeler, D., and Armbruster, T. (1998) Silanol groups in minerals and inorganic compounds. American Mineralogist, 83, 119–125.

Olijnyk, H., Paris, E., Geiger, C.A., and Lager, G.A. (1991) Compressional study of katoite $[Ca_3Al_2(O_4H_4)_3]$ and grossular garnet. Journal of Geophysical Research: Solid Earth, 96, 14313–14318.

O'Neill, B., Bass, J.D., and Rossman, G.R. (1993) Elastic properties of hydrogrossular garnet and implications for water in the upper mantle. Journal of Geophysical Research: Solid Earth, 98, 20031–20037.

Orlando, R., Torres, F., Pascale, F., Ugliengo, P., Zicovich-Wilson, C., and Dovesi, R. (2006) Vibrational spectrum of katoite $Ca_3Al_2[(OH)_4]_3$: a periodic ab initio study. Journal of Physical Chemistry B, 110, 692–701.

827 Pabst, A. (1937) The crystal structure of plazolite. American Mineralogist, 22, 861–868.
828 Pabst, A. (1942) Reexamination of hibschite. American Mineralogist, 27, 783–792.
829 Paier, J., Marsman, M., and Kresse, G. (2007) Why does the B3LYP hybrid functional fail
830 for metals? Journal of Chemical Physics, 127, 024103.
831 Pascale, F., Ugliengo, P., Civalleri, B., Orlando, R., D'Arco, Ph., and Dovesi, R. (2004) The
832 katoite hydrogarnet Si-free $Ca_3Al_2([OH]_4)_3$: A periodic Hartree–Fock and B3-LYP study.
833 Journal of Chemical Physics, 121, 1005–1013.
834 Passaglia, E., and Rinaldi, R. (1984) Katoite, a new member of the $Ca_3Al_2(SiO_4)_3$ -
835 $Ca_3Al_2(OH)_{12}$ series and a new nomenclature for the hydrogrossular group of minerals.
836 Bulletin de Minéralogie, 107, 605–618.
837 Pauling, L. (1929) The principles determining the structure of complex ionic crystals. Journal
838 of the American Chemical Society, 51, 1010–1026.
839 Pickard, C.J., and Needs, R.J. (2011) Ab initio random structure searching. Journal of
840 Physics: Condensed Matter, 23, 053201.
841 Pöllmann, H. (2012) Calcium aluminate cements – Raw materials, Differences, Hydration
842 and Properties. Reviews in Mineralogy and Geochemistry, 74, 1–82.
843 Pòlyà, G., and Read, R.C. (1987) Combinatorial Enumeration of Groups, Graphs, and
844 Chemical Compounds. Springer, New York.
845 Rodehorst, U., Geiger, C.A., and Armbruster, T. (2002) The crystal structures of grossular
846 and spessartine between 100 and 600 K and the crystal chemistry of grossular-spessartine
847 solid solutions. American Mineralogist, 87, 542–549.
848 Sacerdoti, M., and Passaglia, E. (1985) The crystal structure of katoite and implications
849 within the hydrogrossular group of minerals. Bulletin de Minéralogie, 108, 1–8.
850 Sanchez, J., Ducastelle, F., and Gratias, D. (1984) Generalized cluster description of
851 multicomponent systems. Physica A: Statistical Mechanics and its Applications, 128, 334-
852 350.
853 Sanchez, J.M. (1993) Cluster expansions and the configurational energy of alloys. Physical
854 Review B, 48, 14013–14015.
855 Shanno, D.F. (1970) Conditioning of quasi-Newton methods for function minimization.
856 Mathematics of Computation, 24, 647–656.
857 Shannon, R.D., Mariano, A.N., and Rossman, G.R. (1992) Effect of H_2O and CO_2 on
858 Dielectric Properties of Single-Crystal Cordierite and Comparison with Polycrystalline
859 Cordierite. Journal of the American Ceramic Society, 75, 2395–2399.

Taylor, H.F.W., and Newbury, D.E. (1984) An electron microprobe study of a mature cement paste. Cement and Concrete Research, 14, 565–573.

Tilley, C.E. (1957) On the replacement of anorthosite by hydrogrossular in the Transvaal. Trans. Geological Society of South Africa, 60, 15–20.

Vinograd, V., Paulsen, N., Winkler, B., and van de Walle, A. (2010) Thermodynamics of mixing in the ternary rhombohedral carbonate solid solution, $(Ca_xMg_y, Mn_{1-x-y})CO_3$, from atomistic simulations. Calphad, 34, 113 – 119.

Wales, D.J. (1998) Symmetry, near-symmetry and energetics. Chemical Physics Letters, 285, 330 – 336.

Zabinski, W. (1966) Hydrogarnets, vol. 3, pp. 1–61. Pol. Akad. Nauk, Oddzial Krakowie Kom. Nauk Mineral.

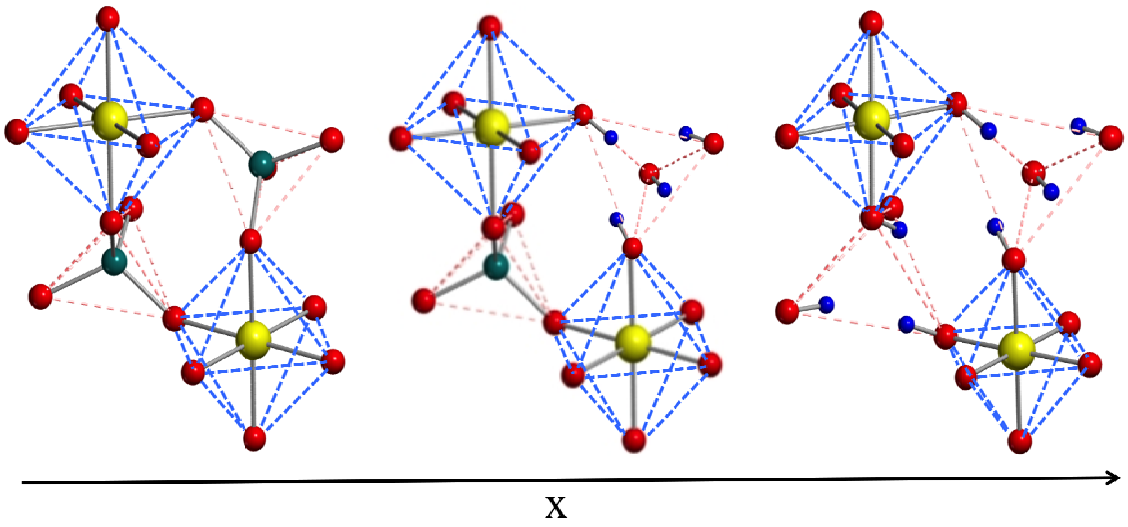

874

875 **Figure 1** (color online) Graphical representation of a portion of the structure of
876 hydrogrossular $Ca_3Al_2(SiO_4)_{3-x}(OH)_{4x}$, as a function of the substitutional fraction *x* of H for
877 Si atoms: pure grossular, $Ca_3Al_2(SiO_4)_3$, on the left; pure silicon-free katoite, $Ca_3Al_2(HO)_{12}$,
878 on the right. Octahedral, AlO_6, and tetrahedral, SiO_4 for grossular and H_4O_4 for katoite,
879 subunits are highlighted with light blue and red dashed lines, respectively. Oxygens in red,
880 silicons in green, aluminums in yellow, hydrogens in blue. Calcium atoms are not shown.

881

882

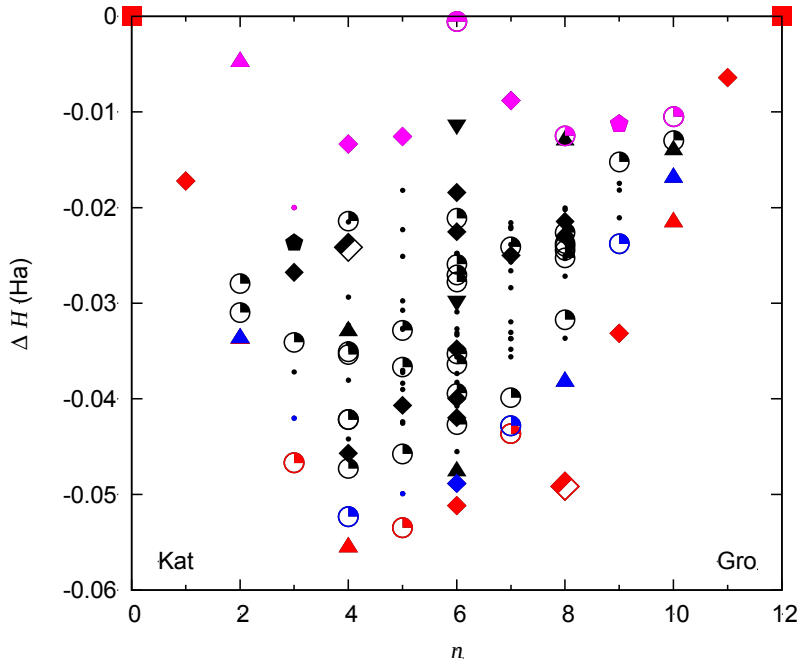

883

884 **Figure 2** (color online) Excess enthalpy ΔH as a function of composition n, which stands for
885 the number of Si atoms in the unit cell. Red and pink points are SICs with minimum and
886 maximum excess enthalpy, respectively; blue points are the SICs with ΔH closest to the
887 minimum; black points are SICs with intermediate excess enthalpy. Different symbols
888 represent different SIC multiplicities M: full square 1; half full circle 2; half full diamond 3;
889 full up triangle 6; full down triangle 8; full diamond 12; full pentagon 16; circle with full
890 quarter 24; small full circle 48.

891

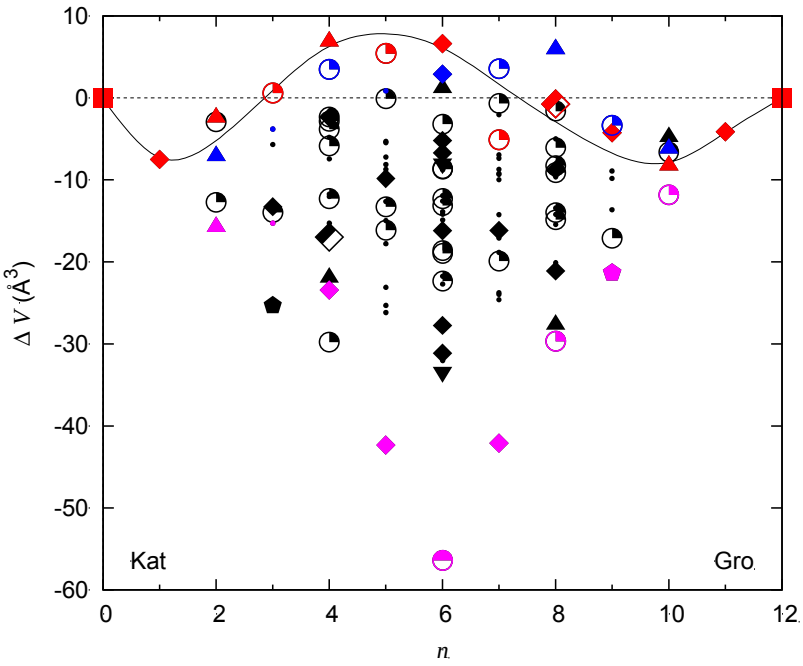

892

893 **Figure 3** (color online) Excess volume ΔV as a function of composition n, which stands for
894 the number of Si atoms in the unit cell. Different colors distinguish the SICs on the basis of
895 the corresponding excess enthalpy, according to the scheme defined in Figure 2. The solid
896 curve is an eye-guide approximating the average function $\Delta\bar{V}(\mathrm{n})$ at 300 K. Different symbols
897 represent different SIC multiplicities M (see caption to Figure 2 for details).

898

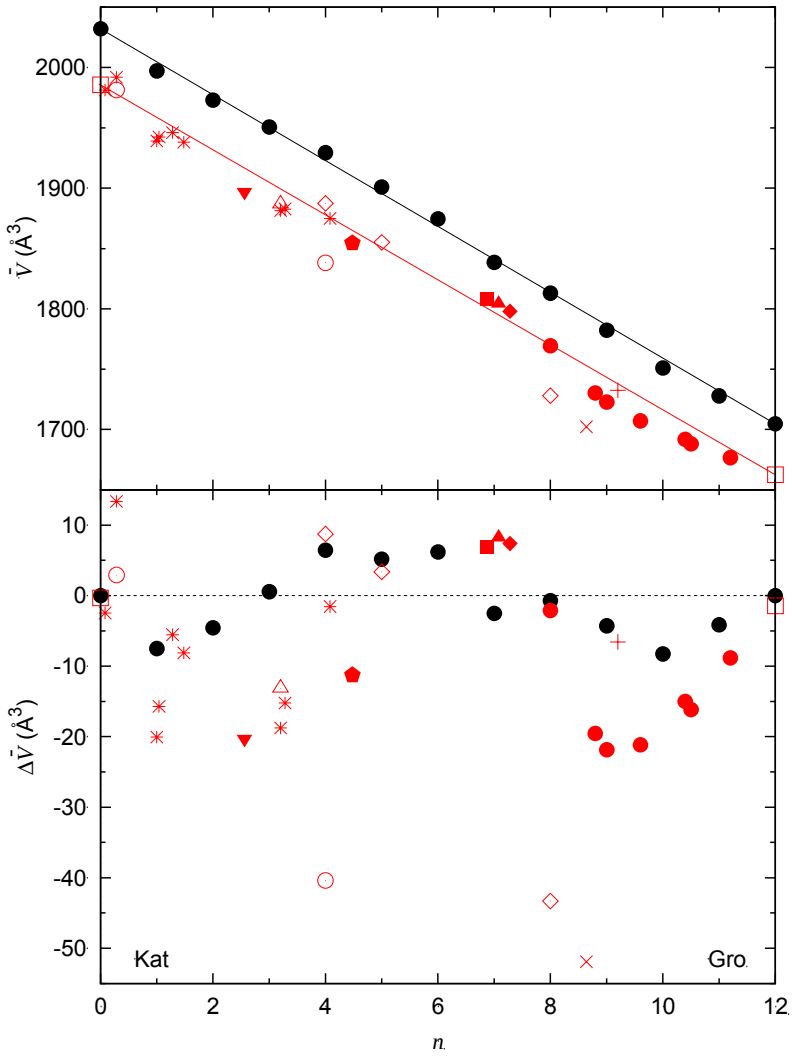

Figure 4 (color online) Boltzmann average volume $\bar{V}$ (upper panel) and excess volume $\Delta\bar{V}$ (lower panel) as functions of the composition n. Full black circles are calculated values at 300 K. Red symbols are experimental data by Pabst (1937), solid rhombus; Flint et al. (1941), empty circles; Cohen-Addad et al. (1967, 1963), cross; Basso et al. (1983), full triangle; Passaglia and Rinaldi (1984), empty triangle; Sacerdoti and Passaglia (1985), full inverted triangle; Lager et al. (1989), plus; Cheng et al. (1990), solid circles; Jappy and Glasser (1991), asterisks; O'Neill et al. (1993), solid square; Ferro et al. (2003), solid pentagon; and Pöllmann (2012), empty rhombi. Empty squares are the end-members obtained as averages of various experiments (Cheng et al. 1990, Cohen-Addad et al. 1963, Flint et al. 1941, Lager et al. 1987a, 2005, 1987b, Novak and Gibbs 1971, Rodehorst et al. 2002). Solid straight lines in the upper panel connect the end-members.

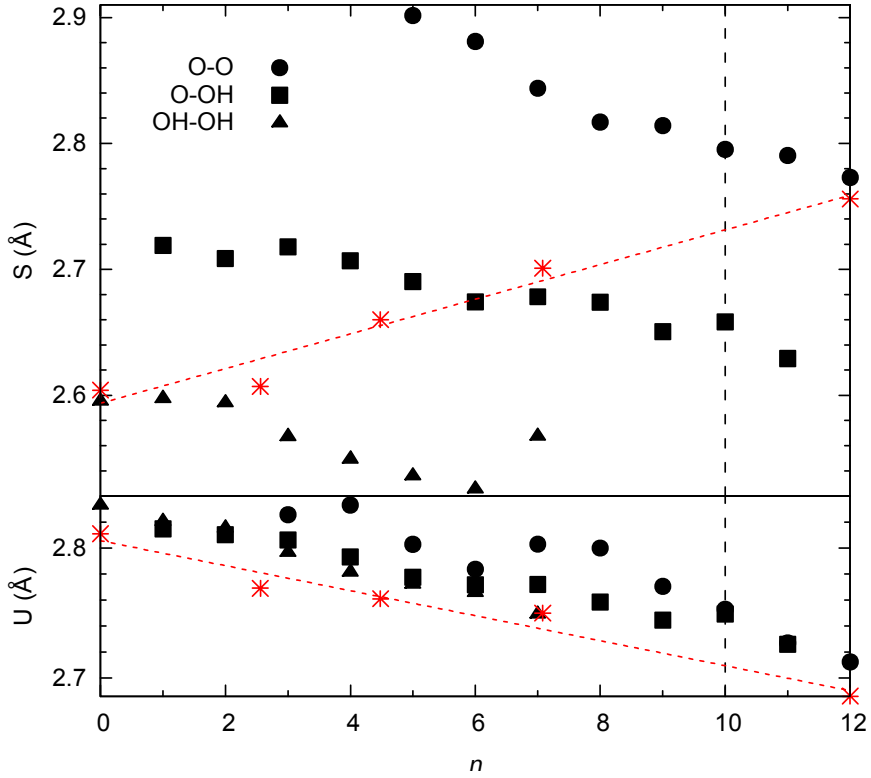

Figure 5 (color online) Octahedral shared, S, and unshared, U, edge length (Å) as a function of composition n. Full symbols represent average values for oxygen pairs $O-O$, $O-OH$ and $OH-OH$. Gray stripes include weighted means over the three oxygen pairs contributing to S and U at the various compositions. The vertical line indicates the composition at which the intersection between the two gray stripes occurs. Red asterisks are experimental data from Lager et al. (1987a), $n = 0$; Sacerdoti and Passaglia (1985), $n = 2.56$; Ferro et al. (2003), $n = 4.48$; Basso et al. (1983), $n = 7.08$; and Novak and Gibbs (1971), $n = 12$.

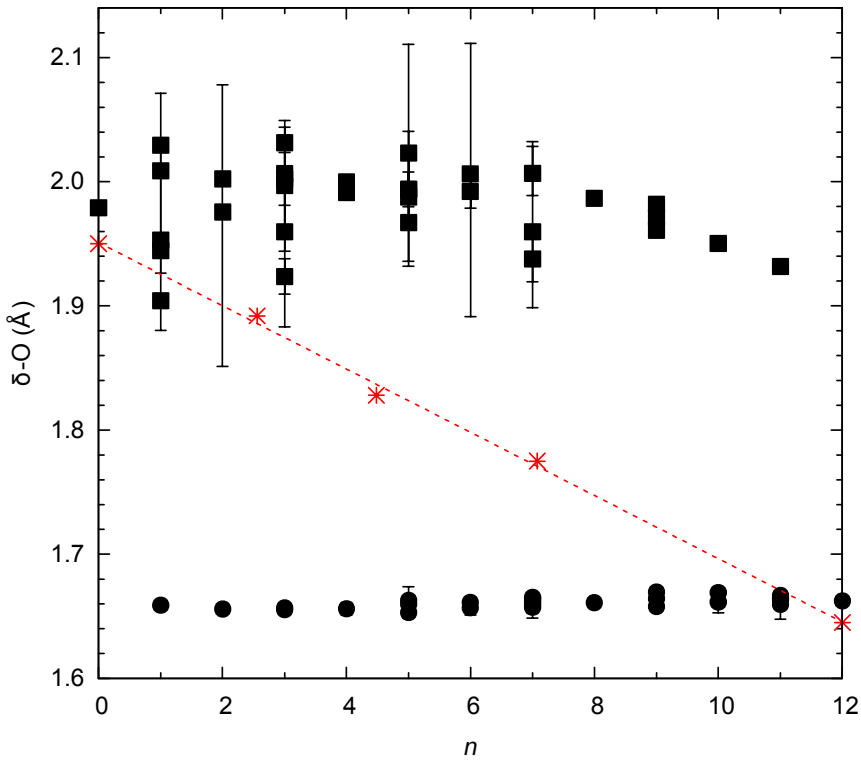

Figure 6 (color online) Tetrahedral δ-O distance (between the barycenter δ and the oxygens at the vertices) as a function of composition n, that is the number of Si atoms in the primitive cell. Full circles and squares are average δ-O values for SiO_4 and H_4O_4 tetrahedra, respectively. Error-bars range from the minimum to the maximum δ-O distance in each tetrahedron. The gray stripe represents average δ-O distances weighted over the SiO_4 and the H_4O_4tetrahedra at each composition. Red asterisks are experimental data from Lager et al. (1987a), $n = 0$; Sacerdoti and Passaglia (1985), $n = 2.56$; Ferro et al. (2003), $n = 4.48$; Basso et al. (1983), $n = 7.08$; and Novak and Gibbs (1971), $n = 12$.

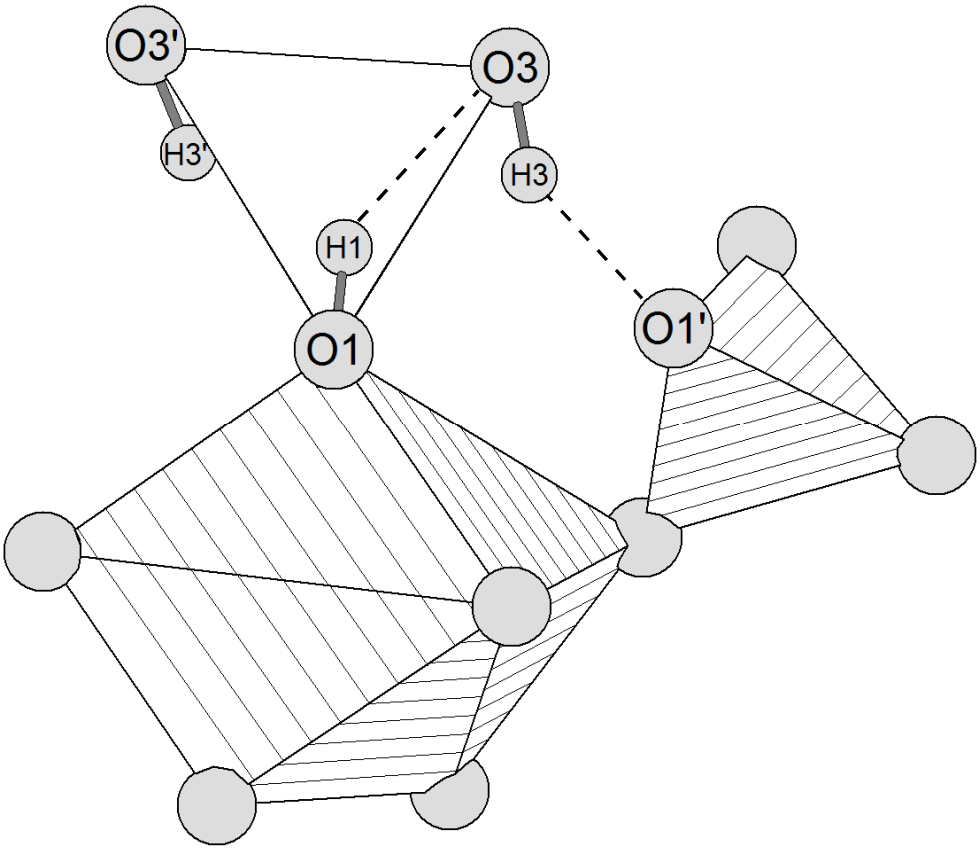

930

931 **Figure 7** Structure drawing of adjacent H_4O_4 and SiO_4 tetrahedra with bridging CaO_8
932 dodecahedron at composition $n = 1$, where n is the number of silicon atoms in the primitive
933 cell. Hydrogen interactions with lengths < 2.5 Å are shown as dashed lines. Atomic labeling
934 notation as in (Novak and Gibbs 1971) and in (Lager et al. 2005). In (Lager et al. 2005) H is
935 replaced by D.

936

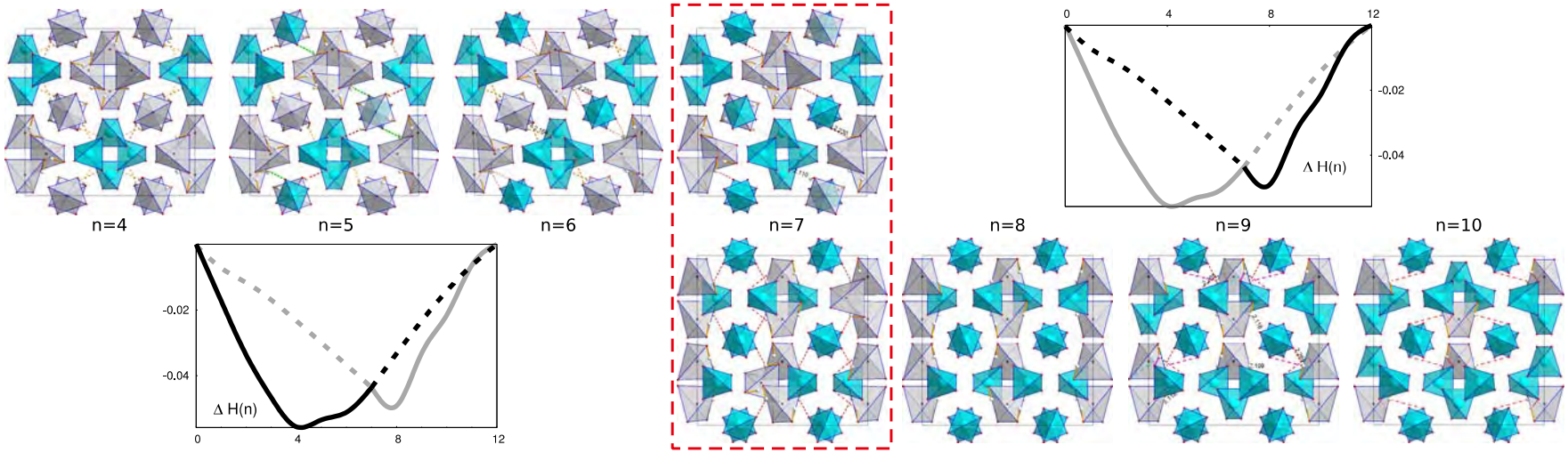

Figure 8 (color online) Distribution of SiO_4 (blue) and H_4O_4 (gray) tetrahedra in the pseudo-cubic cell of minimum energy SICs. The number n of Si atoms refers to the primitive cell. At $n = 7$, two stable SICs with very similar energy are illustrated: the most stable SIC at the bottom, the next one at the top. Two distribution trends are visible, one for $n \leq 7$ and one for $n \geq 7$, in which a structural continuity between the SICs is recognized. Plots of $\Delta H(n)$ (solid lines) feature the two series of SICs in different colors: each color corresponds to a continuity region. $\Delta H(n)$ is likely a superposition of two curves with minima at $n = 4$ and $n = 8$, intersecting at $n = 7$ (discontinuity point). Dashed portions of these curves are drawn as an eye guide.

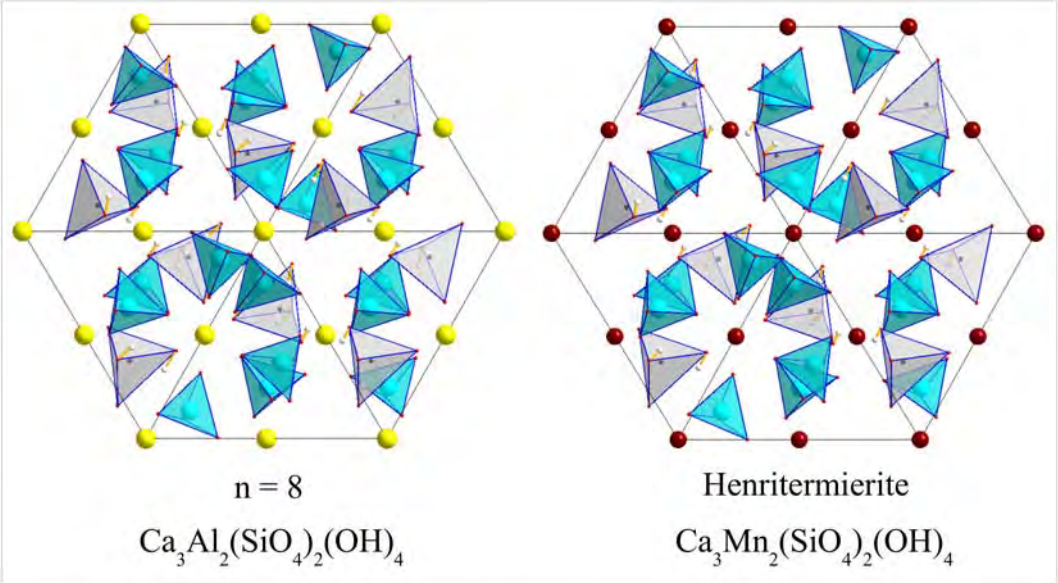

Figure 9 (color online) The tetrahedra distribution of the minimum enthalpy configuration at composition $n = 8$ (left) is compared to that of henritermierite, $Ca_3Mn_2(SiO_4)_2(H_4O_4)$ (right). SiO_4 tetrahedra in blue; H_4O_4tetrahedra in gray. Yellow and brown spheres represent octahedral cations. Note the agreement between calculated and experimental orientation of the $O-H$ groups.

947 **Table I** Distribution of the SICs obtained by substitution of the tetrahedral sites in the garnet
948 primitive cell. For different numbers n of Si atoms, fractional composition $x = 3(1 -$
949 $n/12)$, number of SICs N_{SIC}, total number of atomic configurations N_{Conf}, and minimum
950 multiplicity M_{min}(corresponding to the maximum symmetry) of the respective classes are
951 reported.

n	x	N_{SIC}	N_{Conf}	M_{min}
0	3.00	1	1	1
1	2.75	1	12	12
2	2.50	5	66	6
3	2.25	7	220	12
4	2.00	18	495	3
5	1.75	20	792	12
6	1.50	32	924	2
7	1.25	20	792	12
8	1.00	18	495	3
9	0.75	7	220	12
10	0.50	5	66	6
11	0.25	1	12	12
12	0.00	1	1	1
		136	4096	

952
953

954 **Table II** Lattice parameters a, b, c (Å) and angles α, β, γ (degrees) of the SICs at composition
955 $n = 6$, where n is the number of Si in the primitive cell. The classes are listed in order of
956 increasing energy, the total variation being 51 mHa. Multiplicities M and lattice types (Lat.),
957 as deduced from the analysis of the residual symmetry group, are also reported: Cub = cubic,
958 Tet = tetragonal, Trg = trigonal, Ort = orthorhombic, Mon = monoclinic, Trc = triclinic.
959 Lattice types might not refer to the conventional definition. Percentage indices of the overall
960 deviation from the ideal cubic structure are given at the bottom (see text for definitions).

l	M	a	b	c	α	β	γ	Lat.
1	12	12.324	12.349	12.349	90.00	91.29	90.00	Ort
2	12	12.381	12.294	12.294	90.00	90.00	90.00	Tet
3	6	12.319	12.319	12.320	90.00	90.00	90.00	Tet
4	48	12.358	12.303	12.303	90.61	90.57	90.32	Trc
5	24	12.360	12.360	12.208	89.67	90.33	90.01	Mon
6	12	12.354	12.348	12.214	90.00	90.00	90.00	Ort
7	48	12.339	12.276	12.295	90.46	90.03	89.79	Trc
8	12	12.363	12.321	12.222	90.00	90.00	90.00	Ort
9	24	12.332	12.332	12.204	90.07	89.93	90.05	Mon
10	48	12.322	12.273	12.317	89.51	89.71	90.69	Trc
11	48	12.322	12.310	12.285	89.78	89.29	90.04	Trc
12	24	12.365	12.264	12.264	90.08	90.33	89.67	Mon
13	48	12.324	12.296	12.273	89.71	89.98	90.46	Trc
14	24	12.269	12.312	12.312	89.50	90.70	89.30	Mon
15	12	12.374	12.298	12.171	90.00	90.48	90.00	Mon
16	48	12.334	12.243	12.294	89.96	90.00	90.79	Trc
17	48	12.315	12.314	12.227	90.19	90.29	90.30	Trc
18	48	12.316	12.318	12.234	89.70	89.97	90.11	Trc
19	48	12.313	12.238	12.302	89.92	90.37	90.12	Trc
20	8	12.299	12.299	12.299	89.56	89.56	89.56	Trg
21	48	12.307	12.295	12.256	89.48	90.35	89.90	Trc
22	24	12.324	12.260	12.279	89.66	90.00	90.00	Mon
23	24	12.341	12.242	12.242	89.63	90.03	89.97	Mon
24	24	12.287	12.287	12.227	90.09	89.91	90.30	Mon
25	48	12.315	12.286	12.205	89.78	90.41	89.81	Trc
26	48	12.292	12.304	12.204	89.96	90.30	90.43	Trc
27	12	12.240	12.240	12.287	90.00	90.00	90.00	Tet
28	24	12.286	12.286	12.254	90.03	89.97	90.30	Mon
29	12	12.293	12.225	12.225	90.00	90.00	90.00	Tet
30	48	12.287	12.234	12.216	90.16	90.19	90.13	Trc
31	8	12.243	12.243	12.243	90.39	90.39	90.39	Trg
32	2	12.191	12.191	12.191	90.00	90.00	90.00	Cub
	$\lvert\bar{\Delta}\rvert$	0.27	0.18	0.28	0.22	0.27	0.22	
	$\bar{\Delta}$	0.24	0.00	-0.24	-0.07	0.15	0.08	
	$\max\lvert\Delta\rvert$	0.76	0.41	0.90	0.68	1.43	0.88	

961

962
963
964

965 **Table III** Selected distances (Å) and angles (degrees) involving the hydrogen atom at
966 different compositions n. Minimum energy SICs are considered. Notation as in Figure 7.

n	0	1	4	6	11
$\mathrm{O1-H1}$	0.961	0.961	0.961	0.962	0.963
$\mathrm{O3-H3}$	-	0.969	0.965	0.964	0.963
$\mathrm{H1\cdots O3}$	2.513	2.335	2.547	2.472	2.412
$\mathrm{H1\cdots O3'}$	2.564	2.593	2.553	2.590	2.677
$\mathrm{H3\cdots O1'}$	2.610	2.077	2.172	2.164	2.191
$\mathrm{O1-H1\cdots O3}$	138.8	148.0	147.0	137.7	142.6
$\mathrm{O1-H1\cdots O3'}$	133.2	134.4	133.4	141.5	117.1
$\mathrm{O3-H3\cdots O1'}$	109.0	148.7	132.0	135.9	127.1
$\mathrm{\delta-O1-H1}$	36.26	24.21	27.88	28.55	45.52
$\mathrm{\delta-O3-H3}$	-	65.46	52.17	53.93	45.52

967